Magnetic properties of the triangular lattice magnets $A_4B'B_2O_{12}$ (A=Ba, Sr, La; B'=Co, Ni, Mn; B=W, Re)

R. Rawl,[1] M. Lee,[2,3] E. S. Choi,[3] G. Li,[4] K. W. Chen,[3] R. Baumbach,[3] C. R. dela Cruz,[5] J. Ma,[1,6] and H. D. Zhou[1,3]

[1]*Department of Physics and Astronomy, University of Tennessee, Knoxville, Tennessee 37996-1200, USA*

[2]*Department of Physics, Florida State University, Tallahassee, Florida 32306-3016, USA*

[3]*National High Magnetic Field Laboratory, Florida State University, Tallahassee, Florida 32310-3706, USA*

[4]*School of Physics and Materials Science, Anhui University, Hefei, Anhui 230601, People's Republic of China*

[5]*Quantum Condensed Matter Division, Oak Ridge National Laboratory, Oak Ridge, Tennessee 37831, USA*

[6]*Department of Physics and Astronomy, Shanghai Jiao Tong University, Shanghai 200240, People's Republic of China*

(Received 21 February 2017; revised manuscript received 1 May 2017; published 25 May 2017)

The geometrically frustrated two-dimensional triangular lattice magnets $A_4B'B_2O_{12}$ (A=Ba, Sr, La; B'=Co, Ni, Mn; B=W, Re) have been studied by x-ray diffraction, ac and dc susceptibilities, powder neutron diffraction, and specific-heat measurements. The results reveal the following: (i) The samples containing Co^{2+} (effective spin-1/2) and Ni^{2+} (spin-1) ions with small spin numbers exhibit ferromagnetic (FM) behavior and ordering, respectively, while the sample containing Mn^{2+} (spin-5/2) ions with a large spin number exhibits antiferromagnetic (AFM) ordering. We ascribe these spin-number-manipulated ground states to the competition between the AFM B'-O-O-B' and FM B'-O-B-O-B' superexchange interactions. (ii) The chemical pressure introduced into the Co-containing samples through the replacement of different-size ions on the A site finely tunes the FM behavior temperature of the system. This effect is not simply governed by the lattice parameters and requires more precise structural measurements to elucidate.

DOI: 10.1103/PhysRevB.95.174438

I. INTRODUCTION

Geometrically frustrated magnets have attracted much attention for the novel properties they exhibit at low temperatures such as spin ice, spin liquids, noncollinear ground states, and fractional gauge fields [1–3]. Of particular interest are the two-dimensional (2D) triangular lattice magnets (TLMs) because, despite their simple structure, they can host a multitude of ground states [4–6]. There are several examples: (i) $Ba_3CoSb_2O_9$ [7–10], with an equilateral Co^{2+} (effective spin-1/2) triangular lattice, exhibits a 120° ordered state at zero field and an up-up-down phase with applied field. Although its spin-wave spectrum can be reasonably described by the XXZ model with a weak easy-plane anisotropy, the quantum spin fluctuations still lead to abnormal magnon decay and line broadening that cannot be accounted for by linear and nonlinear spin-wave theories [11]. (ii) $Ba_3BNb_2O_9$ (B=Co [12,13], Ni [14], Mn [15]), $CuCrO_2$ [16,17], and $RbFe(MoO_4)_2$ [18,19] exhibit interesting multiferroic properties in the 120° ordered state; (iii) 2H-$AgNiO_2$ [20,21] is a rare TLM that shows ordering with a collinear alternating stripe pattern which could be related to its strong easy-axis anisotropy; (iv) $AAg_2M(VO_4)_2$ (A=Ba, Sr; M=Co, Ni) [22,23] are TLMs that possess ferromagnetic (FM) orderings due to superexchange via the bridging vanadates on a triangular lattice. (v) $NaVO_2$ [24,25] is a rare TLM exhibiting ordering of the V^{3+} orbitals. Consequently, this orbital ordering relieves the geometrical frustration and leads to long-range magnetic ordering. (vi) Shown recently, the exotic quantum spin liquid (QSL) state is realized in $YbMgGaO_4$ [26–29] with an effective spin-1/2 Yb^{3+} triangular lattice in which the spin anisotropy and next-nearest-neighbor interactions play important roles.

To investigate all of these intriguing ground states, the discovery and exploration of new examples of TLMs are necessary. From a materials engineering perspective, one possible way to realize the 2D triangular lattice is via a stacked layer model, for example, in the perovskite structure [30,31]. The basic perovskite structure (ABO_3) can be considered to consist of three layers of AO_3 with layers of B ions in between. The A- and B-site ions form corner-sharing octahedra with the surrounding oxygen atoms. Alternately, adjacent layers may consist of edge-sharing oxygen octahedra, opening up further stacking mechanisms to be explored in a plethora of compounds [30]. Of interest in realizing true 2D behavior is the presence of vacant layers in which neither a magnetic nor nonmagnetic ion resides. This vacancy helps to ensure that interlayer interactions are small compared to intralayer interactions.

Based on this principle, we examine 2D TLMs utilizing close-packed stacking of perovskite layers. A promising structure is $A_4B'B_2O_{12}$ (A=Ba, Sr, La; B'=Co, Ni, Mn; B=W, Re). In this structure, using $A_4CoB_2O_{12}$ as an example in Fig. 1, the magnetic Co^{2+} ions and nonmagnetic W^{6+}/Re^{7+} ions occupy the octahedral sites in the perovskite layers in an ordered fashion at the 3*a* and 6*c* positions, respectively. Thus, the CoO_6 ocatahedral layer forms a Co^{2+} triangular lattice in the *ab* plane. Here the Co octahedra are corner sharing with the adjacent W/Re octahedra, and this Co layer is sandwiched by two $(W/Re)O_6$ layers. Moreover, the octahedral interstices between the two adjacent W/Re layers are vacant to accommodate the strong electric repulsion of the W^{6+}/Re^{7+} ions. The separation of the layers of Co^{2+} by two layers of W^{6+}/Re^{7+} and one vacant layer significantly reduces the interplane interactions and enhances the 2D nature of this structure. More intriguingly, due to the flexible chemistry in this structure, we can easily introduce chemical pressure into the system by changing the lattice parameters. For example, within the set of samples $Sr_4CoRe_2O_{12}$, $Sr_2La_2CoW_2O_{12}$, $Ba_2La_2CoW_2O_{12}$, $Ba_3LaCoReWO_{12}$, and $Ba_4CoRe_2O_{12}$, we expect the lattice parameters will change accordingly as we

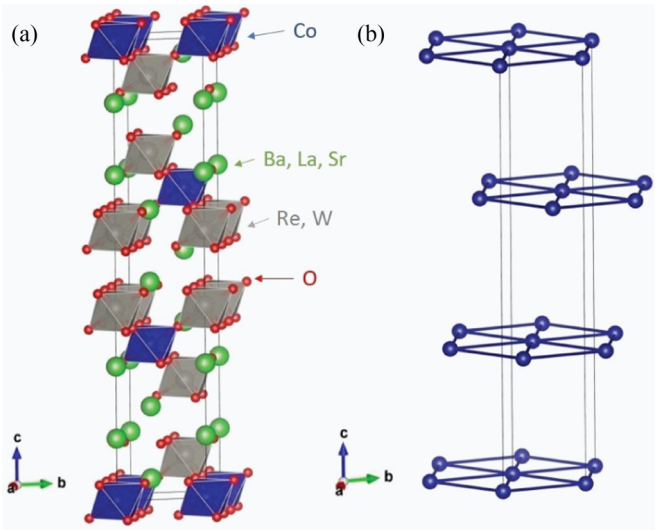

FIG. 1. (a) Crystalline structure of $A_4CoB_2O_{12}$ with the space group *R-3mH*. (b) Staggered pattern of triangular Co^{2+} planes along the *c* axis.

replace Sr^{2+} ions with larger La^{2+} and even larger Ba^{2+} ions. We can also easily change the spin numbers of the system by varying the magnetic B' ions. For example, within the set of samples $Ba_2La_2CoW_2O_{12}$, $Ba_2La_2NiW_2O_{12}$, and $Ba_2La_2MnW_2O_{12}$, the spin numbers change from effective spin 1/2 (Co^{2+}) to spin 1 (Ni^{2+}) and spin 5/2 (Mn^{2+}). Therefore, the $A_4B'B_2O_{12}$ structure provides an ideal platform to study the magnetic properties of new TLMs and how the perturbations, such as chemical pressure and spin numbers, affect them. So far, while the structures of several $A_4B'B_2O_{12}$ members have been reported [32–34] and the susceptibility of $Ba_2La_2MnW_2O_{12}$ [35] has been measured down to 2 K, there are no detailed studies on their magnetic properties.

In this paper, we examine the structural and magnetic properties of seven members of $A_4B'B_2O_{12}$ by using x-ray diffraction (XRD), ac and dc susceptibilities (χ_{AC}, χ_{DC}), neutron powder diffraction (NPD), and specific-heat (C_P) measurements. The results reveal that the nature of the magnetic ground state is governed by spin size. For low spin, the compounds are FM, with B'=Ni showing FM long-range ordering (LRO) and B'=Co showing FM behavior. For high spin (B'=Mn), the compound possesses AFM LRO. We propose that this ground-state change is due to the competition between two different superexchange interactions present in the structure.

II. EXPERIMENT

In total, seven polycrystalline samples of $A_4B'B_2O_{12}$ were prepared using the standard solid-state reaction method. They are $Sr_4CoRe_2O_{12}$, $Sr_2La_2CoW_2O_{12}$, $Ba_2La_2CoW_2O_{12}$, $Ba_3LaCoReWO_{12}$, $Ba_4CoRe_2O_{12}$, $Ba_2La_2NiW_2O_{12}$, and $Ba_2La_2MnW_2O_{12}$. Stoichiometric amounts of $BaCO_3/SrCO_3$, La_2O_3 (predried at 980 °C overnight), $CoCO_3/NiO/MnO$, and WO_3/Re powders were mixed in agate mortars, compressed into pellets, and annealed for 20 h at temperatures of 1000 °C for $Ba_4CoRe_2O_{12}$, 1050 °C for $Ba_3LaCoReWO_{12}$,

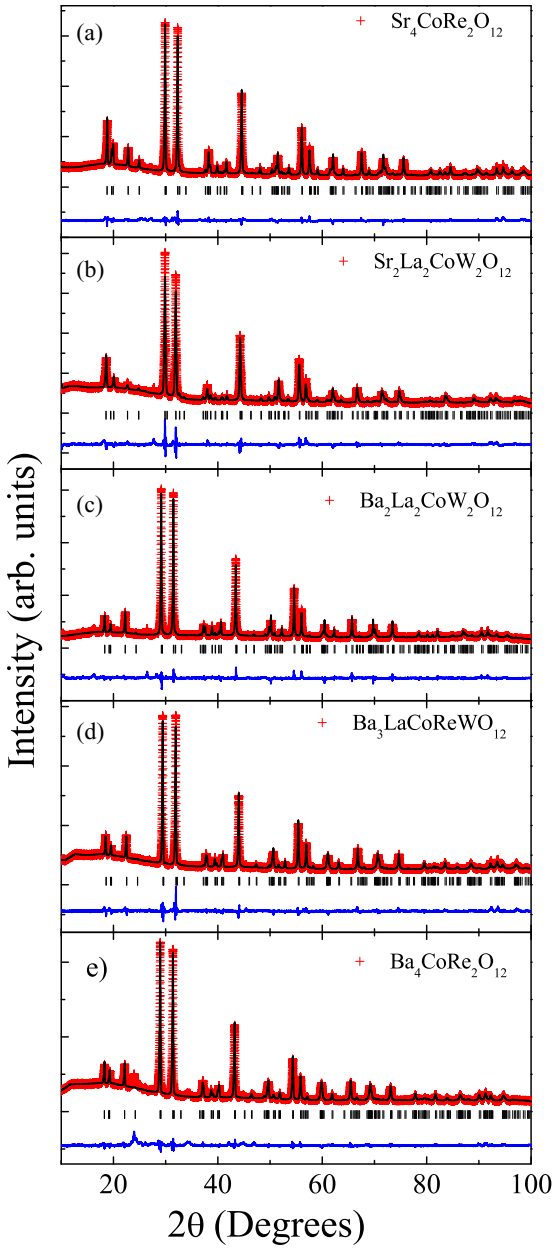

FIG. 2. (a)–(e) Powder x-ray diffraction patterns (red crosses) and Rietveld refinements (black line) for five $A_4CoB_2O_{12}$ compounds. The blue line at the bottom of each panel is the difference curve. The black ticks are the reflection positions.

1100 °C for $Sr_4CoRe_2O_{12}$, and 1250 °C for $Ba_2La_2CoW_2O_{12}$, $Sr_2La_2CoW_2O_{12}$, $Ba_2La_2MnW_2O_{12}$, and $Ba_2La_2NiW_2O_{12}$.

Powder XRD patterns were performed at room temperature using a HUBER imaging-plate Guinier camera 670 with Ge monochromatized Cu $K\alpha_1$ radiation (1.54059 Å). High-resolution neutron powder diffraction measurements were performed by a neutron powder diffractometer, HB2A, at the High Flux Isotope Reactor (HFIR) of the Oak Ridge National Laboratory (ORNL). Around 3 g of powder were loaded in an Al-cylinder can and mounted in a close-cycled refrigerator. We used a neutron wavelength of $\lambda = 1.5405$ Å with a collimation of 12′-open-6′. Both the XRD and NPD patterns were analyzed by the Rietveld refinement program

TABLE I. Structural parameters for the Co-containing compounds at room temperature (space group *R-3mH*) determined from refined XRD measurements.

Refinement	Atom	Site	x	y	z	Occupancy
$Sr_4CoRe_2O_{12}$,[a] $\chi^2 = 2.29$	Sr1	6c	0	0	0.12982(5)	0.16666
	Sr2	6c	0	0	0.29351(6)	0.16666
	Co	3a	0	0	0	0.08333
	Re	6c	0	0	0.42186(3)	0.16667
	O1	18h	0.50289(50)	0.49711(50)	0.12312(14)	0.50
	O2	18h	0.49249(53)	0.50751(53)	0.29174(19)	0.50
$Sr_2La_2CoW_2O_{12}$,[b] $\chi^2 = 5.41$	Sr	6c	0	0	0.13664(13)	0.16667
	La	6c	0	0	0.28914(8)	0.16667
	Co	3a	0	0	0	0.08333
	W	6c	0	0	0.42105(8)	0.16667
	O1	18h	0.50728(82)	0.49272(82)	0.12425(22)	0.50
	O2	18h	0.48772(73)	0.51228(73)	0.29016(28)	0.50
$Ba_2La_2CoW_2O_{12}$, [c] $\chi^2 = 3.45$	Ba	6c	0	0	0.13467(8)	0.16667
	La	6c	0	0	0.29032(7)	0.16667
	Co	3a	0	0	0	0.08333
	W	6c	0	0	0.41635(7)	0.16667
	O1	18h	0.50913(77)	0.49087(77)	0.11994(23)	0.50
	O2	18h	0.48361(62)	0.51639(62)	0.29662(28)	0.50
$Ba_3LaCoWReO_{12}$, [d] $\chi^2 = 1.43$	Ba1	6c	0	0	0.12939(6)	0.12500
	La1	6c	0	0	0.12944(6)	0.04167
	Ba2	6c	0	0	0.29533(6)	0.12500
	La2	6c	0	0	0.29533(6)	0.04167
	Co	3a	0	0	0	0.08333
	W	6c	0	0	0.42185(6)	0.08333
	Re	6c	0	0	0.42185(6)	0.08333
	O1	18h	0.51068(82)	0.48932(82)	0.12143(23)	0.50
	O2	18h	0.48365(80)	0.51635(80)	0.29260(32)	0.50
$Ba_4CoRe_2O_{12}$, [e] $\chi^2 = 4.51$	Ba1	6c	0	0	0.12911(8)	0.16666
	Ba2	6c	0	0	0.29435(9)	0.16666
	Co	3a	0	0	0	0.08333
	Re	6c	0	0	0.42089(8)	0.16667
	O1	18h	0.50262(108)	0.49738(108)	0.12325(29)	0.50
	O2	18h	0.47513(97)	0.52487(97)	0.28794(41)	0.50

[a] $a = b = 5.54464(26)$ Å, $c = 26.73815(126)$ Å, overall B factor $= 1.332$ Å^2.
[b] $a = b = 5.60493(41)$ Å, $c = 26.58453(197)$ Å, overall B factor $= 2.211$ Å^2.
[c] $a = b = 5.68043(12)$ Å, $c = 27.37418(60)$ Å, overall B factor $= 2.671$ Å^2.
[d] $a = b = 5.70429(9)$ Å, $c = 27.675722(54)$ Å, overall B factor $= 1.757$ Å^2.
[e] $a = b = 5.72455(33)$ Å, $c = 27.76966(161)$ Å, overall B factor $= 1.694$ Å^2.

FULLPROF [36]. The dc magnetic susceptibility measurements were performed at temperatures of 2–300 K using a Quantum Design superconducting interference device magnetometer with an applied field of 0.5 T. The ac susceptibility was measured with the conventional mutual inductance technique with a homemade setup [37]. The specific-heat data were obtained using a commercial physical property measurement system (Quantum Design).

III. RESULTS

Cobalt-containing compounds. The refined XRD patterns of five Co-containing compounds are shown in Fig. 2. All compounds show pure phases with the space group *R-3mH*. Used as a continuing example, $Sr_4CoRe_2O_{12}$ has lattice constants of $a = 5.5446(3)$ Å and $c = 26.7382(13)$ Å. The refined structural parameters are listed in Table I. It is clear that the lattice parameters are governed by the size of *A*-site ions, with cell volume increasing as strontium is replaced by lanthanum and subsequently replaced by barium. We also tested the refinement by involving the site mixing between Co and W/Re sites. However, the refinements with the extra variable show no improvement from the refinement of the fully ordered structure used here. The results indicate that the site disorder in the compounds is not significant. It could be below 5% within our XRD resolution.

The inverse dc susceptibilities for all five Co-containing members are shown in Figs. 3(a)–3(e). All $1/\chi_{DC} \sim T$ curves show a slope change around 80 K. Continuing to use $Sr_4CoRe_2O_{12}$ as an example, linear fitting from 150 to

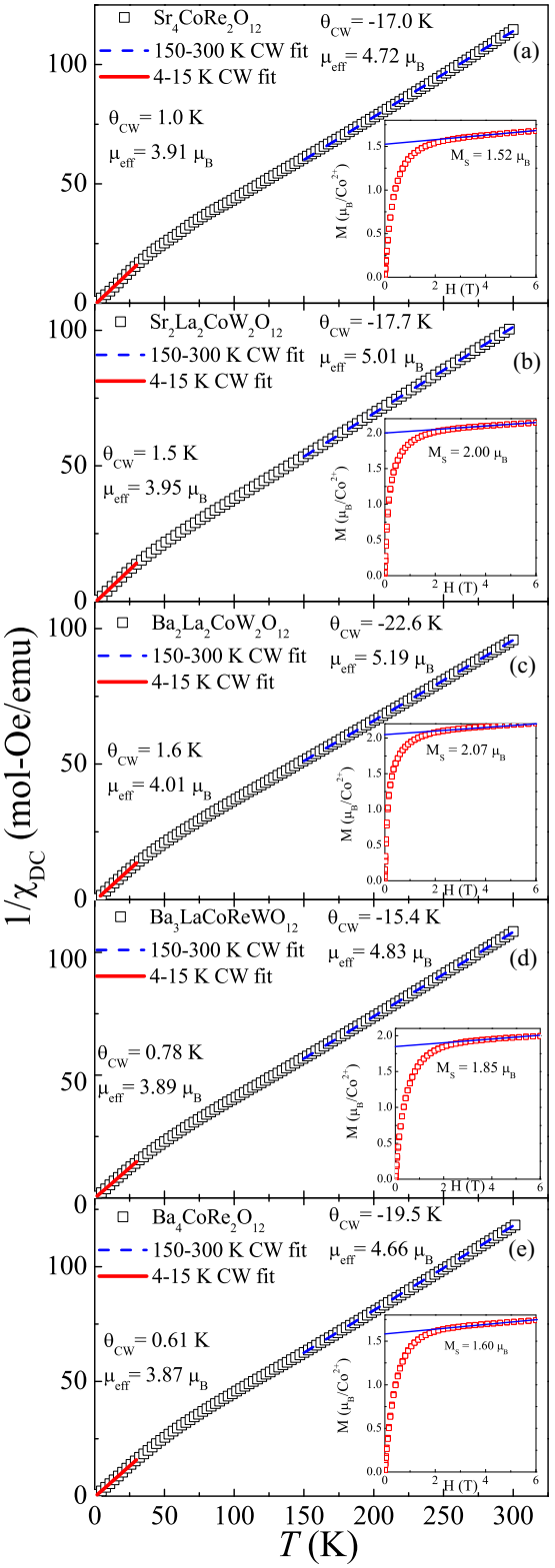

FIG. 3. (a)–(e) The inverse dc susceptibility of the $A_4CoB_2O_{12}$ compounds. The solid and dashed lines are Curie-Weiss fittings of the low-temperature and high-temperature regimes, respectively. Insets: dc magnetization taken at 1.8 K. The saturation magnetization of the Co^{2+} ion is extrapolated using a linear fit to account for the Van Vleck paramagnetic contribution.

TABLE II. Summary of magnetic properties: FM behavior, FM transition, and AFM transition temperatures T_{FM}, T_C, T_N, Curie-Weiss constant θ_{CW}, effective magnetic moment μ_{eff}, saturation magnetization M_S, and gyromagnetic ratio g of $A_4B'B_2O_{12}$ compounds.

Compound	$T_{FM}/T_C/T_N$ (K)	θ_{CW} (K)	μ_{eff} (μ_B)	M_S (μ_B)	g
$Sr_4CoRe_2O_{12}$	1.0	1.0	3.91	1.5	3.0
$Sr_2La_2CoW_2O_{12}$	1.26	1.5	3.95	2.0	4.0
$Ba_2La_2CoW_2O_{12}$	1.28	1.6	4.01	2.1	4.2
$Ba_3LaCoReWO_{12}$	0.83	0.78	3.89	1.9	3.8
$Ba_4CoRe_2O_{12}$	0.87	0.61	3.87	1.6	3.2
$Ba_2La_2NiW_2O_{12}$	6.2	25.5	3.19	≈2	≈2
$Ba_2La_2MnW_2O_{12}$	1.7	−10.7	5.73		

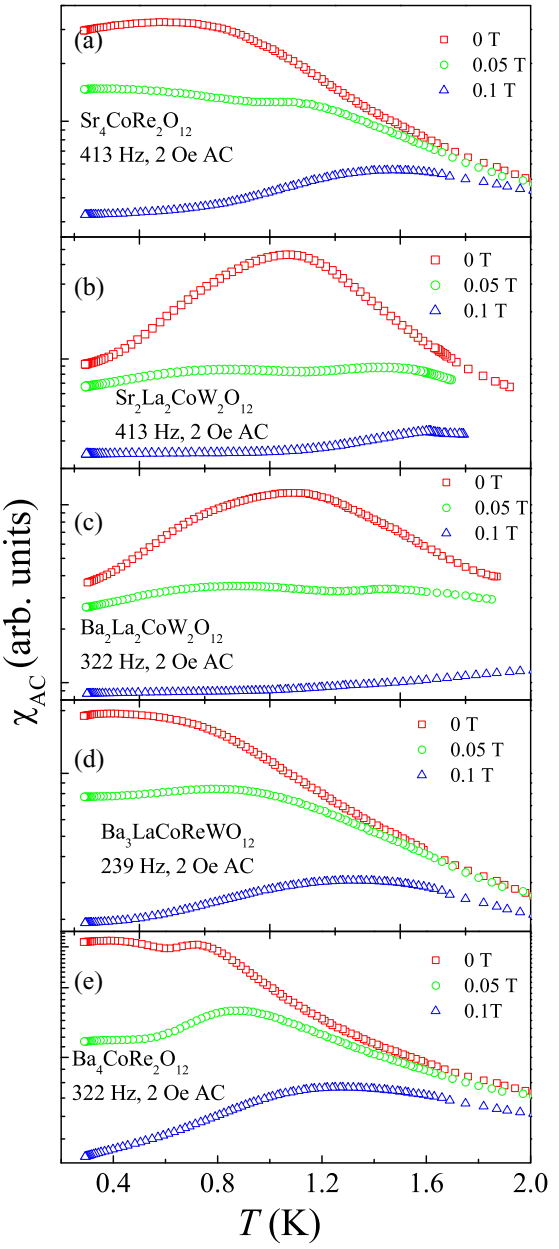

FIG. 4. (a)–(e) The real part of the ac susceptibility χ_{AC} for cobalt containing $A_4B'B_2O_{12}$ compounds measured from 0.3 to 2.0 K under different dc magnetic fields. Excitation fields of 2 Oe at low ac frequencies were used.

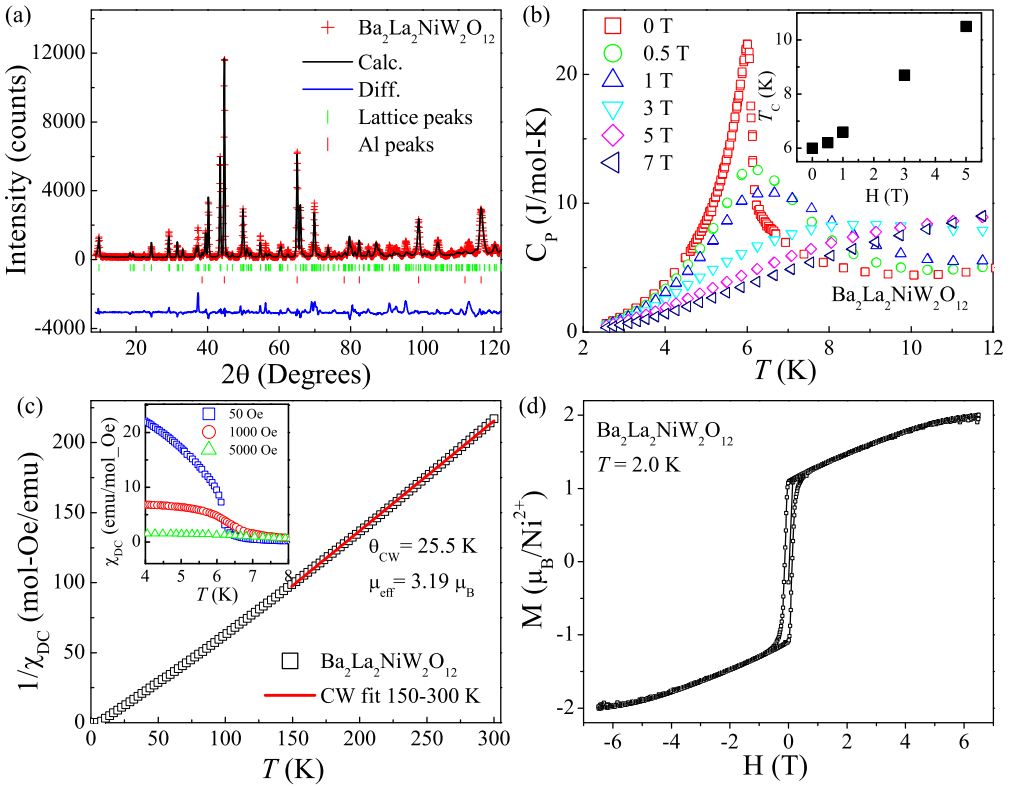

FIG. 5. For $Ba_2La_2NiW_2O_{12}$, (a) the Rietveld refinement of the NPD pattern measured at room temperature using a neutron wavelength of $\lambda = 1.5405$ Å. (b) The temperature dependence of C_P measured at different dc fields. Inset: the field dependence of T_C. (c) The inverse dc susceptibility. The solid line is the linear fitting. Inset: the temperature dependence of dc susceptibility measured under different fields. (d) The dc magnetization curve measured at 2 K.

300 K yields a Curie-Weiss constant of $\theta_{CW} = -17$ K and $\mu_{eff} = 4.72\mu_B$, while the linear fitting from 4.0 to 15 K yields $\theta_{CW} = 1.0$ K and $\mu_{eff} = 3.91\mu_B$. This change in effective magnetic moment indicates a spin-state transition of the Co^{2+} ions from high spin ($S = 3/2$) to low spin ($S = 1/2$). This transition is due to the octahedral environment of the Co^{2+} ions, where the combination of the crystal field and spin-orbital coupling leads to a Kramers doublet ground state with effective $S = 1/2$, as described by Low [38] and further examined by Lloret *et al.* [39]. Thus, the positive θ_{CW} at low temperatures suggests FM exchange interactions of the effective spin-1/2 Co^{2+} ions. The spin-state transition and positive θ_{CW} were also observed for the four other Co compounds with similar linear fittings. The dc magnetization data were taken at 1.8 K, shown

TABLE III. Structural parameters for $Ba_2La_2NiW_2O_{12}$ and $Ba_2La_2MnW_2O_{12}$ at room temperature (space group *R-3mH*) determined from refined NPD measurements.

Refinement	Atom	Site	*x*	*y*	*z*	Occupancy
$Ba_2La_2NiW_2O_{12}$[a]	Ba	6c	0	0	0.13324(60)	0.16667
	La	6c	0	0	0.29309(44)	0.16667
	Ni	3a	0	0	0	0.08333
	W	6c	0	0	0.41881(68)	0.16667
	O1	18h	0.49760(81)	0.50240(81)	0.11707(27)	0.50
	O2	18h	0.47868(74)	0.52132(74)	0.29302(37)	0.50
$Ba_2La_2MnW_2O_{12}$[b]	Ba	6c	0	0	0.13551(85)	0.16667
	La	6c	0	0	0.29341(47)	0.16667
	Mn	3a	0	0	0	0.08333
	W	6c	0	0	0.41653(86)	0.16667
	O1	18h	0.49847(95)	0.50153 (95)	0.11839(30)	0.50
	O2	18h	0.47415(88)	0.52586(88)	0.29343(38)	0.50

[a] $a = b = 5.66221(40)$ Å, $c = 27.36606(224)$ Å, overall B factor $= 1.401$ Å^2.
[b] $a = b = 5.72804(74)$ Å, $c = 27.38715(384)$ Å, overall B factor $= 1.558$ Å^2.

in the insets of Figs. 3(a)–3(e). All data consistently show a tendency of saturation around $\mu_0 H_s \approx 3$ T. To account for Van Vleck paramagnetism, a linear fit of high-field data was used to calculate the saturation magnetization M_S. For $Sr_4CoRe_2O_{12}$, the extrapolation yields a value of $M_S = 1.52\mu_B/Co^{2+}$ and a powder-averaged gyromagnetic ratio $g = 3.04$. For the four other compounds, the obtained g is around 3–4.2. All of the magnetic parameters are summarized in Table II.

The real part of the ac susceptibility measurements taken under different dc fields for the Co compounds is shown in Fig. 4. Continuing to use $Sr_4CoRe_2O_{12}$ as an example, its χ_{AC} shows a fast increase with decreasing temperature below 1.5 K followed by a broad peak. This feature, while not strong enough evidence to claim LRO, is evidence for FM behavior such as the formation of FM clusters or FM correlations. Here we define the FM behavior temperatures T_{FM} as the local minimum position in the first derivative of χ_{AC}, which is 1.0 K for $Sr_4CoRe_2O_{12}$. With increasing dc field, this broad peak shifts to higher temperatures while simultaneously decreasing in magnitude. This increase in T_{FM} under applied field further indicates a FM nature, which is consistent with the dc susceptibility results. The four other Co compounds show similar χ_{AC} behavior with different T_{FM}, which are listed in Table II. Therefore, all five Co compounds show FM behavior around 1 K. One noteworthy feature is that for $Sr_2La_2CoW_2O_{12}$ and $Ba_2La_2CoW_2O_{12}$, χ_{AC} shows a second peak at lower temperatures below 1 K when a 0.05 T dc field is applied. Whether this feature represents further FM behavior requires further exploration.

$Ba_2La_2NiW_2O_{12}$. The Rietveld refinement performed on the NPD pattern [Fig. 5(a)] measured at room temperature confirms the pure phase with space group *R-3mH* for $Ba_2La_2NiW_2O_{12}$. The refined structural parameters are $a = 5.6622(4)$ Å and $c = 27.3661(22)$ Å. The detailed structural parameters are listed in Table III. Under zero field, the specific-heat data [Fig. 5(b)] show a sharp peak at 6.2 K, in agreement with T_C from χ_{DC}. Under applied dc fields, this peak broadens out and occurs at higher temperatures. The transition temperature (the peak position) increases linearly with the increasing field, as shown in the inset of Fig. 5(b). The linear fitting of the inverse dc susceptibility from 150 to 300 K [Fig. 5(c)] yields a positive $\theta_{CW} = 25.5$ K and $\mu_{eff} = 3.19\mu_B$, indicating FM interactions. As shown in the inset of Fig. 5(c), the χ_{DC} measured at 50 Oe clearly shows a sharp transition at $T_C = 6.2$ K (defined as the minimum in $d\chi_{DC}/dT$). With increasing field, this transition becomes broader and shifts to higher temperatures, which again verifies its FM nature. The dc magnetization data taken at 2.0 K [Fig. 5(d)] clearly show a hysteresis loop and a saturation value at $M_S \approx 2\,\mu_B$. NPD performed at 2 and 20 K shows clear magnetic Bragg peaks overlapping lattice Bragg peaks (Fig. 6), confirming the onset of FM LRO. Refinement of the ferromagnetic contribution results in a magnetic moment of $\approx 2\mu_B$, consistent with the magnetization data. Due to the powder nature of the sample, the spin orientation cannot be resolved. All of these data, such as the peak of C_P and fast increase in χ_{DC} at 6.2 K, the positive θ_{CW}, the hysteresis loop of magnetization, the increase in T_C under fields, and magnetic Bragg peaks from NPD, consistently show that $Ba_2La_2NiW_2O_{12}$ is a spin-1 system with long-range FM ordering at 6.2 K.

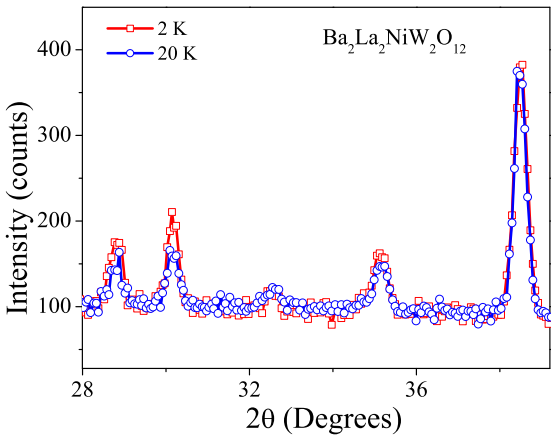

FIG. 6. NPD of $Ba_2La_2NiW_2O_{12}$ taken at 2 and 20 K. The overlap of magnetic Bragg peaks with lattice Bragg peaks indicates FM long-range ordering.

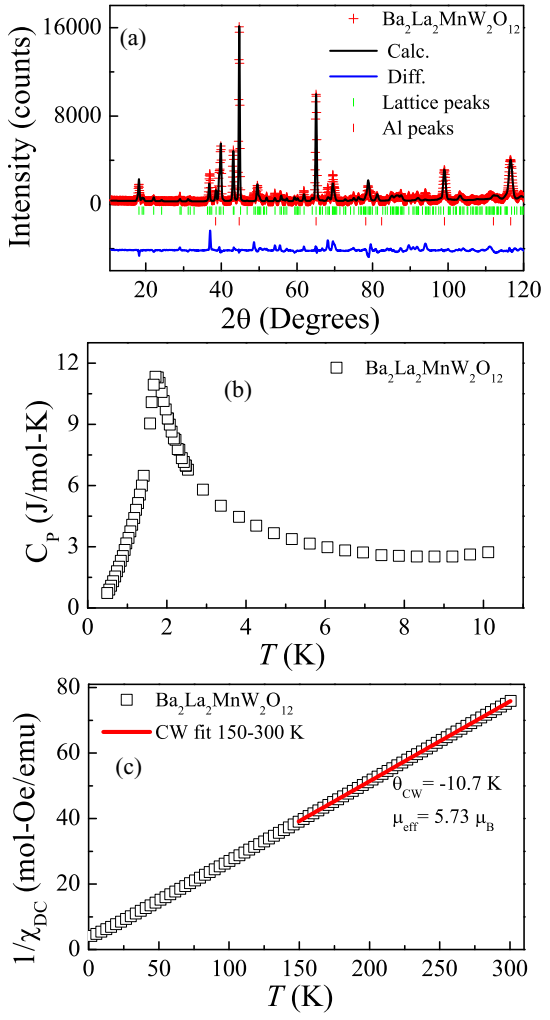

FIG. 7. For $Ba_2La_2MnW_2O_{12}$, (a) the Rietveld refinement of the NPD pattern taken at room temperature. (b) The temperature dependence of C_P measured at zero field. (c) The inverse dc susceptibility. The solid line is the linear fitting.

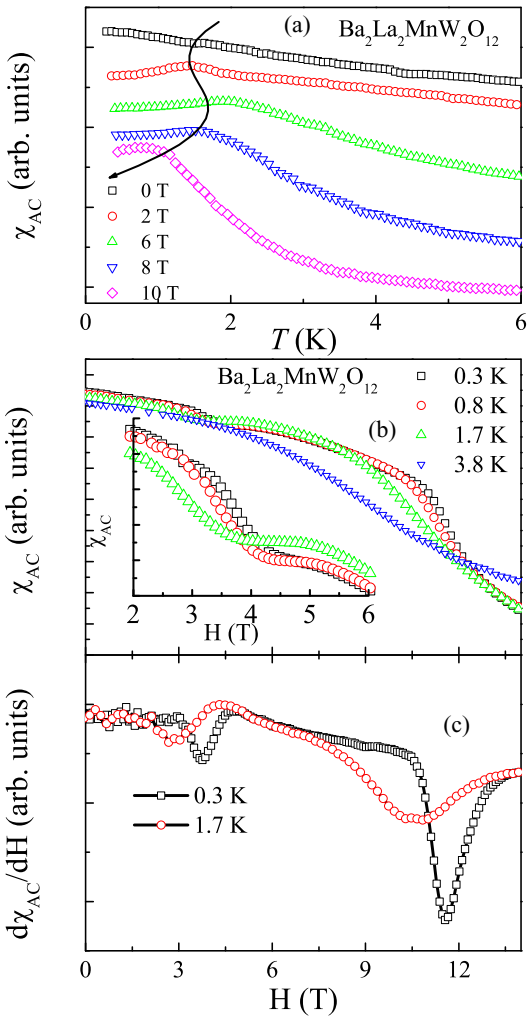

FIG. 8. (a) The temperature dependence of χ_{AC} for $Ba_2La_2MnW_2O_{12}$ under applied dc fields. (b) The dc field dependence of χ_{AC} at various temperatures. Inset: the enlargement of the data around 4 T. (c) The derivative of the field dependence of χ_{AC} at different temperatures.

$Ba_2La_2MnW_2O_{12}$. The Rietveld refinement performed on the NPD pattern measured at room temperature [Fig. 7(a)] confirms the pure phase with space group *R-3mH* for $Ba_2La_2MnW_2O_{12}$. The refined structural parameters are $a = 5.7280(4)$ Å and $c = 27.3872(38)$ Å. The detailed structural parameters are listed in Table III. The specific-heat data [Fig. 7(b)] show a sharp peak at $T_N = 1.7$ K, which should represent AFM long-range ordering. The linear fitting of the inverse dc susceptibility from 150 to 300 K [Fig. 7(c)] yields a negative $\theta_{CW} = -10.7$ K and $\mu_{eff} = 5.73\mu_B$, indicating AFM interactions.

The susceptibility χ_{AC} was measured as a function of temperature under varying applied dc fields [Fig. 8(a)] and as a function of dc field under applied temperatures [Fig. 8(b)]. Here transitions were again found using local minima of $d\chi_{AC}/dT$ and $d\chi_{AC}/dH$. As shown in Fig. 8(a), at zero field, the temperature dependence of χ_{AC} shows no significant feature but a weak slope change around 1.7 K, which is consistent with T_N observed from the specific heat. Then, with

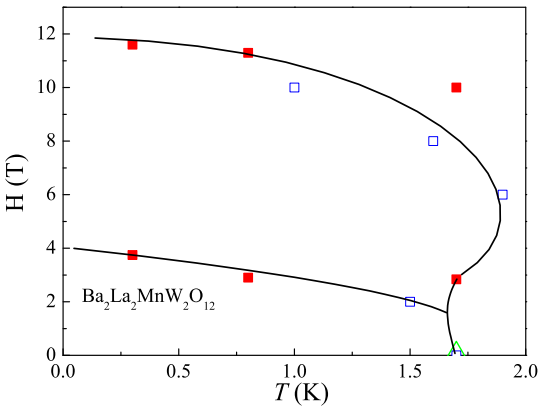

FIG. 9. Magnetic phase diagram of $Ba_2La_2MnW_2O_{12}$. Transition temperatures were found from the temperature derivative (red solid squares), the field derivative (blue open squares) of χ_{AC}, and zero-field C_P measurements (green triangle).

$H = 2$ T, there is a peak that appears at 1.5 K. Thereafter, this peak position shifts to higher temperatures first and then shifts to lower temperatures with increasing dc field, as indicated by the curved arrow in Fig. 8(a). Meanwhile, the field scan performed at 0.3 K shows two slope changes around 4 and 11 T. These two features are more clearly visible as the two sharp valleys from the $d\chi_{AC}/dH$ curve [Fig. 8(c)]. Here we define the minima positions as $H_{c1} = 3.75$ T and $H_{c2} = 11.6$ T. With increasing temperature, these two features become broader and shift to lower fields. Above T_N, they disappear. A magnetic phase diagram of $Ba_2La_2MnW_2O_{12}$ was constructed by the transition temperatures and critical field values obtained from C_P and χ_{AC}, as shown in Fig. 9.

IV. DISCUSSION

It is obvious that the spin number of the magnetic B' ions significantly affects the magnetic ground states of the studied $A_4B'B_2O_{12}$ compounds, which manifest FM ordering for the Co^{2+} ($S = 1/2$) and Ni^{2+} ($S = 1$) compounds but AFM ordering for the Mn^{2+} ($S = 5/2$) compound. To understand this drastic ground-state change, we examine the superexchange interactions of the B'^{2+} ions in the structure. Using the theoretical framework laid down by Kanamori [40], a qualitative description of the superexchange interaction between magnetic cations on an octahedral site can be determined from the orbital configurations of the magnetic cations and the nonmagnetic, bridging anions. In $A_4B'B_2O_{12}$, octahedra of $B'O_6$ are corner sharing with octahedra of BO_6 via an oxygen atom, providing two pathways for intralayer superexchange. These paths are B'^{2+}-O^{2-}-O^{2-}-B'^{2+} and B'^{2+}-O^{2-}-W^{6+}-O^{2-}-B'^{2+} or B'^{2+}-O^{2-}-Re^{7+}-O^{2-}-B'^{2+}, as shown in Fig. 10(a). The superexchange pathway along B'^{2+}-O^{2-}-O^{2-}-B'^{2+} is commonly found in other magnetic oxides, where the interaction is AFM.

Meanwhile, for W^{6+} and Re^{7+} ions on octahedral sites, the cubic crystal field splits their degenerate $4f$ orbitals (the filled outermost orbitals) into three groups, as shown in Fig. 10(b). The group of f_{x^3}, f_{y^3}, and f_{z^3} with t_{1g} symmetry mainly participates in the orbital hybridization with the O^{2-}

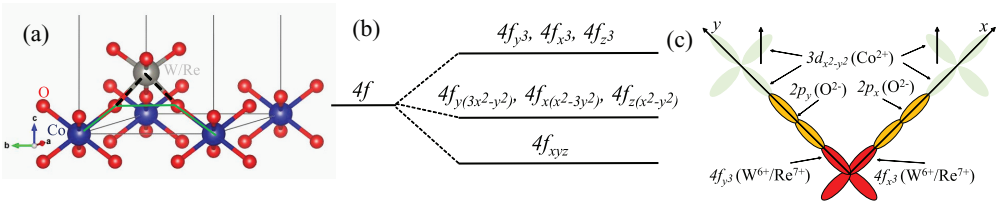

FIG. 10. (a) Pathways for FM B'-O-B-O-B' (black dashed line) and AFM B'-O-O-B' (green solid line) superexchange interactions. (b) Energy levels of $4f$ orbitals in cubic symmetry, with the highest energy levels having the same symmetry as p orbitals. (c) Orbital diagram of FM B'-O-B-O-B' interaction with f orbitals represented by symmetrically similar p orbitals.

$2p$ orbitals due to geometrical reasons. Thus, one possible situation for the B'^{2+}-O^{2-}-W^{6+}-O^{2-}-Cr^{3+} exchange path, which is similar for the Re case, is shown in Fig. 10(c). Here we consider the superexchange interaction between the spins on the $d_{x^2-y^2}$ orbitals of the B'^{2+} ions and assume that the B'^{2+}, O^{2-}, and W^{6+} ions are on the same line and that the O^{2-}-W^{6+}-O^{2-} bond angle is 90°. In this situation, spin 1 on the left B'^{2+} ion is transferred to the molecular orbital composed of the p_y orbitals of the O^{2-} $2p$ orbitals and the f_{y^3} orbitals of the W^{6+} $4f$ orbitals; meanwhile, spin 2 on the right B'^{2+} ion is transferred to the molecular orbital composed of the p_x orbitals of O^{2-} and the f_{x^3} orbitals of W^{6+} ions. Due to Hund's rules, these two spins on the f_{y^3} and f_{x^3} orbitals in the W^{6+} ions have to be parallel. Then, after these two spins are transferred back to the B'^{2+} ion, a FM superexchange interaction between them is formed. With these two different superexchanges in the system, it is natural to propose that the ground-state change is due to the competition between them. This means the FM interaction exceeds the AFM interaction for spin-1/2 and −1 systems, but AFM interactions are stronger for the spin-5/2 system.

Since the t_{1g} symmetry of the $4f$ orbitals here is identical to the symmetry of the p orbitals of $4p$ or $3p$ orbitals, similar FM superexchange interactions should also occur for $3d$-$2p$-$4p$ (or $3p$)-$2p$-$3d$ paths. Several other TLMs with layered perovskite structures have been observed to possess such FM superexchange interactions. Similar competitive FM and AFM superexchanges are observed in $Ba_3CoNb_2O_9$ [13], where the Co^{2+}-O^{2-}-Nb^{5+}-O^{2-}-Co^{2+} superexchange interaction involving the Nb^{5+} $4p$ orbitals is FM, and it opposes the AFM Co^{2+}-O^{2-}-O^{2-}-Co^{2+} interaction, leading to a weaker AFM interaction. This manifests in a low AFM transition temperature as well as a low saturation field. Alternatively, $AAg_2M(VO_4)_2$ (A=Ba, Sr; M=Co, Ni) [22] has a stronger FM superexchange via Co^{2+}-O^{2-}-V^{5+}-O^{2-}-Co^{2+} than AFM superexchange via Co^{2+}-O^{2-}-O^{2-}-Co^{2+} and possesses an FM transition.

Next, we look into the chemical pressure effect among the Co samples. In general, the increasing lattice parameter should decrease the exchange interactions and therefore lead to a lower T_{FM}. However, that is not the case here. Instead, with increasing lattice parameter, T_{FM} first increases from Sr_4 to Sr_2La_2 and then to the Ba_2La_2 sample; afterwards, it decreases to Ba_3La and to the Ba_4 sample. To explore the more general rule behind this chemical pressure effect, we must turn to more detailed structural information. Figure 11 shows that there is no structural distortion upon cooling from the high-spin ($S = 3/2$) to low-spin ($S = 1/2$) states of the Co^{2+} ion. Thus, the substitution of A-site ions will provide isostructural chemical pressure, as seen in the XRD refinements, even at low temperatures. Unfortunately, the angle of the O-B-O bond cannot be resolved sufficiently with the available XRD resolution. Further neutron studies will be pursued to examine if there is further evidence to explain the fine-tuning of the Co sample FM behavior temperature.

Finally, we comment on the phase diagram of $Ba_2La_2MnW_2O_{12}$. One common ground state at zero field observed for studied triangular lattice antiferromagnets (TLAFs), such as $Ba_3CoSb_2O_9$ [7] and $Ba_3BNb_2O_9$ (B=Co [12,13], Ni [14], Mn [15]), is the 120° ordered state. The phase diagrams of these TLAFs consistently show canted 120°, up-up-down, oblique, and polarized phases with increasing applied magnetic field. Comparing the phase diagram of $Ba_2La_2MnW_2O_{12}$ to the reported diagrams for $Ba_3CoSb_2O_9$ and $Ba_3BNb_2O_9$, the overall trend is similar. Therefore, we tend to ascribe the zero-field ground state of $Ba_2La_2MnW_2O_{12}$ to 120° ordering. With increasing field, it enters the canted 120° phase below H_{c1}, the up-up-down phase above H_{c1}, and then the polarized phase above H_{c2}. One difference here is that we do not observe the oblique phase boundary between the up-up-down and polarized phases for $Ba_2La_2MnW_2O_{12}$. One possibility is that our ac measurements do not have the resolution to detect this phase boundary due to the polycrystalline nature of the sample.

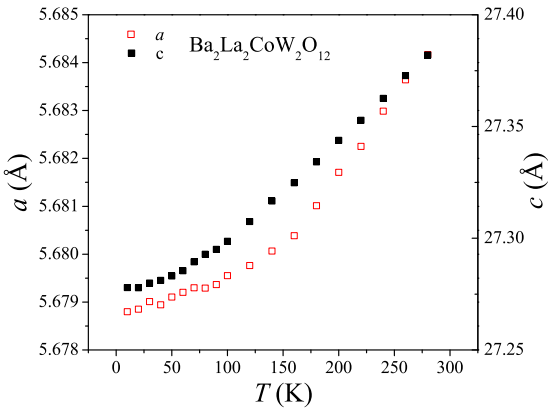

FIG. 11. Temperature dependence of lattice parameters a and c for $Ba_2La_2CoW_2O_{24}$. No structural distortion is seen upon the transition from high spin ($S = 3/2$) to low spin ($S = 1/2$) of the Co^{2+} ions.

V. CONCLUSION

We have examined the structural and magnetic properties of a family of $A_4B'B_2O_{12}$ compounds with a 2D magnetic triangular lattice. Due to the competition between two kinds of superexchange interactions (one FM and one AFM) in the structure, the ground states of the triangular lattice can be efficiently tuned by varying the spin numbers of the magnetic B'^{2+} ions. The result is FM behavior and ordering for the Co and Ni samples, respectively, with small spin numbers and AFM ordering for the Mn samples with a large spin number. Moreover, the chemical pressure can finely tune the FM behavior temperature and effective exchange interactions among the Co sample via a mechanism remaining to be explored. These findings demonstrate that $A_4B'B_2O_{12}$ is a platform for TLMs waiting for future exploration to study geometrically frustrated magnetism.

ACKNOWLEDGMENTS

R.R. and H.D.Z. are grateful for the support from NSF DMR through Grant No. DMR-1350002. J.M. is grateful for the support of the Ministry of Science and Technology of China (Grant No. 2016YFA0300500). The research at HFIR/ORNL was sponsored by the Scientific User Facilities Division, Office of Basic Energy Sciences, and U.S. Department of Energy. The work at NHMFL is supported by NSF Grant No. DMR-1157490 and the state of Florida.

[1] A. P. Ramirez, Annu. Rev. Mater. Sci. **24**, 453 (1994).
[2] L. Balents, Nature (London) **464**, 199 (2010).
[3] J. Greedan, J. Mater. Chem. **11**, 37 (2000).
[4] M. F. Collins and O. A. Petrenko, Can. J. Phys. **75**, 605 (1997).
[5] A. V. Chubukov and D. I. Golosov, J. Phys. Condens. Matter **3**, 69 (1991).
[6] O. A. Starykh, W. Jin, and A. V. Chubukov, Phys. Rev. Lett. **113**, 087204 (2014).
[7] H. D. Zhou, C. Xu, A. M. Hallas, H. J. Silverstein, C. R. Wiebe, I. Umegaki, J. Q. Yan, T. P. Murphy, J.-H. Park, Y. Qiu, J. R. D. Copley, J. S. Gardner, and Y. Takano, Phys. Rev. Lett. **109**, 267206 (2012).
[8] T. Susuki, N. Kurita, T. Tanaka, H. Nojiri, A. Matsuo, K. Kindo, and H. Tanaka, Phys. Rev. Lett. **110**, 267201 (2013).
[9] G. Quirion, M. Lapointe-Major, M. Poirier, J. A. Quilliam, Z. L. Dun, and H. D. Zhou, Phys. Rev. B **92**, 014414 (2015).
[10] G. Koutroulakis, T. Zhou, Y. Kamiya, J. D. Thompson, H. D. Zhou, C. D. Batista, and S. E. Brown, Phys. Rev. B **91**, 024410 (2015).
[11] J. Ma, Y. Kamiya, T. Hong, H. B. Cao, G. Ehlers, W. Tian, C. D. Batista, Z. L. Dun, H. D. Zhou, and M. Matsuda, Phys. Rev. Lett. **116**, 087201 (2016).
[12] M. Lee, J. Hwang, E. S. Choi, J. Ma, C. R. Dela Cruz, M. Zhu, X. Ke, Z. L. Dun, and H. D. Zhou, Phys. Rev. B **89**, 104420 (2014).
[13] K. Yokota, N. Kurita, and H. Tanaka, Phys. Rev. B **90**, 014403 (2014).
[14] J. Hwang, E. S. Choi, F. Ye, C. R. Dela Cruz, Y. Xin, H. D. Zhou, and P. Schlottmann, Phys. Rev. Lett. **109**, 257205 (2012).
[15] M. Lee, E. S. Choi, X. Huang, J. Ma, C. R. Dela Cruz, M. Matsuda, W. Tian, Z. L. Dun, S. Dong, and H. D. Zhou, Phys. Rev. B **90**, 224402 (2014).
[16] H. Kadowaki, H. Kikuchi, and Y. Ajiro, J. Phys. Condens. Matter **2**, 4485 (1990).
[17] K. Kimura, H. Nakamura, K. Ohgushi, and T. Kimura, Phys. Rev. B **78**, 140401 (2008).
[18] M. Kenzelmann, G. Lawes, A. B. Harris, G. Gasparovic, C. Broholm, A. P. Ramirez, G. A. Jorge, M. Jaime, S. Park, Q. Huang, A. Ya. Shapiro, and L. A. Demianets, Phys. Rev. Lett. **98**, 267205 (2007).
[19] A. B. Harris, Phys. Rev. B **76**, 054447 (2007).
[20] E. Wawrzyńska, R. Coldea, E. M. Wheeler, I. I. Mazin, M. D. Johannes, T. Sörgel, M. Jansen, R. M. Ibberson, and P. G. Radaelli, Phys. Rev. Lett. **99**, 157204 (2007).
[21] E. M. Wheeler, R. Coldea, E. Wawrzyńska, T. Sörgel, M. Jansen, M. M. Koza, J. Taylor, P. Adroguer, and N. Shannon, Phys. Rev. B **79**, 104421 (2009).
[22] A. Möller, N. E. Amuneke, P. Daniel, B. Lorenz, C. R. dela Cruz, M. Gooch, and P. C. W. Chu, Phys. Rev. B **85**, 214422 (2012).
[23] A. A. Tsirlin, A. Möller, B. Lorenz, Y. Skourski, and H. Rosner, Phys. Rev. B **85**, 014401 (2012).
[24] T. M. McQueen, P. W. Stephens, Q. Huang, T. Klimczuk, F. Ronning, and R. J. Cava, Phys. Rev. Lett. **101**, 166402 (2008).
[25] T. Jia, G. R. Zhang, Z. Zeng, and H. Q. Lin, Phys. Rev. B **80**, 045103 (2009).
[26] Y. Li, G. Chen, W. Tong, L. Pi, J. Liu, Z. Yang, X. Wang, and Q. Zhang, Phys. Rev. Lett. **115**, 167203 (2015).
[27] Y. Li, H. Liao, Z. Zhang, S. Li, F. Jin, L. Ling, L. Zhang, Y. Zou, L. Pi, Z. Yang, J. Wang, Z. Wu, and Q. Zhang, Sci. Rep. **5**, 16419 (2015).
[28] Y. Shen, Y. D. Li, H. Wo, Y. Li, S. Shen, B. Pan, Q. Wang, H. C. Walker, P. Steffens, M. Boehm, Y. Hao, D. L. Quintero-Castro, L. W. Harriger, M. D. Frontzek, L. Hao, S. Meng, Q. Zhang, G. Chen, and J. Zhao, Nature (London) **540**, 559 (2016).
[29] J. A. M. Paddison, M. Daum, Z. Dun, G. Ehlers, Y. Liu, M. B. Stone, H. D. Zhou, and M. Mourigal, Nat. Phys. **13**, 117 (2016).
[30] L. Katz and R. Ward, Inorg. Chem. **3**, 205 (1964).
[31] A. Maignan, W. Kobayashi, S. Hébert, G. Martinet, D. Pelloquin, N. Bellido, and Ch. Simon, Inorg. Chem. **47**, 8553 (2008).
[32] J. M. Longo, L. Katz, and R. Ward, Inorg. Chem. **4**, 235 (1965).
[33] H. J. Rother, A. Fadini, and S. Kemmler-Sack, Z. Anorg. Allg. Chem **463**, 137 (1980).
[34] S. Kemmler-Sack, Z. Anorg. Allg. Chem **461**, 142 (1980).
[35] Z. F. Li, J. L. Sun, L. P. You, Y. X. Wang, and J. H. Lin, J. Alloys Compd. **379**, 117 (2004).
[36] J. Rodriguez-Carvajal, Phys. B (Amsterdam, Neth.) **192**, 55 (1993).
[37] Z. L. Dun, M. Lee, E. S. Choi, A. M. Hallas, C. R. Wiebe, J. S. Gardner, E. Arrighi, R. S. Freitas, A. M. Arevalo-Lopez, J. P. Attfield, H. D. Zhou, and J. G. Cheng, Phys. Rev. B **89**, 064401 (2014).
[38] W. Low, Phys. Rev. **109**, 256 (1958).
[39] F. Lloret, M. Julve, J. Cano, R. Ruiz-García, and E. Pardo, Inorg. Chim. Acta. **361**, 3432 (2008).
[40] J. Kanamori, J. Phys. Chem. Solids **10**, 87 (1959).